

Towards single-molecule nanomechanical mass spectrometry

A. K. Naik^{*1}, M. S. Hanay^{*1}, W. K. Hiebert^{*1,2}, X. L. Feng¹, M. L. Roukes^{†1}

¹ Kavli Nanoscience Institute, California Institute of Technology, MC 114-36, Pasadena, CA 91125 USA

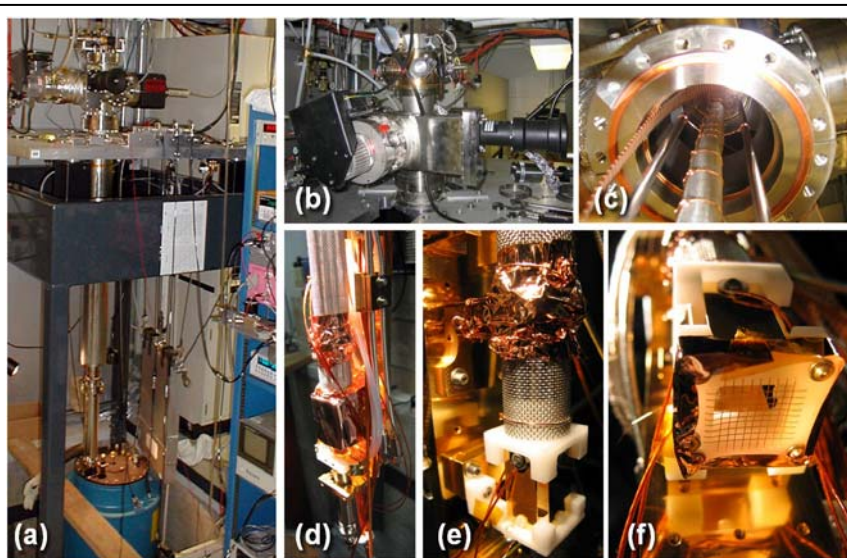
² National Institute for Nanotechnology, National Research Council of Canada, Edmonton, Alberta T6G 2M9 Canada

NEMS-MS System Overview

We employ proven methodologies from state-of-the-art mass spectrometry to build a novel MS system using ultra high frequency NEMS mass sensors. Components include a room-temperature, atmospheric pressure electrospray ionization (ESI) system for creating protein ions or charged nanoparticles, a two-stage differential vacuum system, RF hexapole ion optics to guide the charged analytes to the detector, and the NEMS mass detector stage. These are assembled to form a hybrid system comprising both custom built and commercial instrumentation.

Figure S1 is a montage of images depicting our first experimental prototype system for NEMS-MS enabling the introduction, transport, and mass measurements on individual proteins and nanoparticles. Protein ions or charged nanoparticles are produced using electrospray ionization (ESI) and delivered to a hexapole ion guide driven at radio frequencies (RF), which then transports these species to the NEMS mass sensor with minimal m/z discrimination, as desired. The detection circuitry utilizes a bridge circuit to null the background near the NEMS

Figure S1. First Generation NEMS-MS System. (a) The cryostat, its vibration isolation & support system, and (in pit) the super-conducting magnet, and its dewar. (b) Electrospray ionization unit at top of system. (c) Hexapole ion guide from bottom. (d)(e) Sample stage region; progressive magnifications. (f) Hexapole ion guide; outlet detail.



*These authors contributed equally to this work.

resonance¹⁻³ and a frequency-modulated, phase-locked loop (FM-PLL) to track the NEMS resonant frequency in real time⁴.

Biological sample preparation

Bovine Serum Albumin (BSA), β -Amylase and 5-nm (nominal) diameter colloidal gold nanoparticles were obtained from Sigma-Aldrich and used without further purification. The solutions employed for ESI are as follows:

1. Bovine Serum Albumin (Mol. Wt.=66kDa) : 25 μ M solution in 95/5 v% H₂O/HAc
2. β -Amylase (Mol. Wt.=200kDa) : 0.2 μ M in pH~6.5 10mM NH₄Ac buffer in 50/50 v% H₂O/MeOH
3. Sigma-Aldrich colloidal gold nanoparticle solution (G1402) diluted ten-fold by 50/50 v% H₂O/MeOH

Electrospray Injection (ESI) and differential vacuum assembly

Protein ions and charged nanoparticles are produced using a commercial electrospray ionization (ESI) system (Varian). ESI is one of two well known “soft” ionization processes that can reliably bring large macromolecules from the solution phase into the vapor phase^{5,6}.

These solutions were introduced using a syringe pump (Harvard Apparatus) and syringes (Hamilton) to the electrospray needle (Agilent) by direct infusion through standard MS components (Upchurch) to achieve typical flow rates of 4 μ L/min. High-voltage sources (Emco) are used to bias the ESI needle at a constant voltage of ~2.5-3kV. Solvated analytes delivered to the needle are forced out in the form of charged droplets that repel each other due to coulombic forces^{5,6}. The solvent within these droplets evaporates, reducing their volume yet preserving the amount of charge contained. The increasingly unstable microdroplets eventually undergo “coulomb fission”, fragmenting into daughter droplets, and repeated cycles of this process ultimately result in the formation of bare ionized proteins. Although the exact mechanism of protein ion formation from small droplets is still under debate⁷, electrospray has become a well-established technique for producing proteins in vapor form.

Our ESI delivery system is built around a commercial sub-assembly (Varian 1200 LC/MS) and comprises the following components:

- 1) An ESI needle and gas sheath mounted in an outer chamber at atmospheric pressure and room temperature.
- 2) A 1st vacuum stage with a shield plate, counterflow gas path, capillary, and pumping port.
- 3) A 2nd vacuum stage including a skimmer, collisional-cooling hexapole (“top hexapole”), and final high vacuum orifice. This sub-assembly is embedded in a custom 2nd stage vacuum chamber designed for about 10 mTorr base pressure for optimal collisional cooling^{8,9} of the ions. It is then attached to the top plate of the high-vacuum cryostat chamber housing the “bottom hexapole” (see below) and the NEMS sample stage.

All N₂ gas, vacuum port, electronic, and fluidic lines are connected to external instrumentation.

[†] Corresponding author: roukes@caltech.edu

Ion transport

Electrospray ionization is typically performed at atmospheric pressure and at room, or elevated, temperature. This enables the solvent droplets that form beyond the Taylor cone to quickly evaporate leaving the bare protein ions they contain. In this first-generation NEMS-MS realization we employ physisorption to capture and immobilize the analytes on the NEMS sensor's surface. By contrast, this requires that the NEMS be maintained under high-vacuum and low temperature conditions. Our experimental setup must therefore provide a match between these rather different conditions; we achieve this with a combination of commercially-available and custom-built cryogenic and differential-pumping components. In our first-generation design the NEMS sample stage is located about 2m away from the ESI source. Since the capture area of the NEMS sensor is small, this necessitates efficient transport of the analyte ions created by electrospray to guide them along a 2m path to the surface of the NEMS sensor for adsorption.

Transport of ions from atmospheric pressure to the first differential pumping stage is performed through the so called nozzle-skimmer configuration^{10,11}. This produces a highly collinear, monochromatic beam of nitrogen molecules and protein ions. Subsequently, the ions are transported from this initial vacuum stage to the NEMS sensor by a hexapole ion guide system, having an outer radius of ~ 1.2 cm and total length of ~ 2 m. The hexapole configuration was chosen as a good compromise between obtaining high transmission efficiency and providing

Parameter	Description	Typical Values
V_{needle}	Voltage on the electrospray needle	3.0kV
V_{L4}	Voltage on the electrostatic lens between top and bottom hexapole	-20V
V_{shield}	Voltage on the shield (ESI counter electrode)	600V
$V_{\text{capillary}}$	Voltage on the capillary	200V
$V_{\text{top_hex}}$	DC offset voltage on the top hexapole	10V
$V_{\text{bot_hex}}$	DC offset voltage on the bottom hexapole	0V
f_{RF}	RF frequency of AC voltage applied to the hexapole	1.1MHz, 450kHz
V_{RF}	Amplitude of the RF voltage applied to hexapole	500V
P_{int}	Pressure in the intermediate collisional focusing chamber	8mTorr
T_{dry}	Temperature of the drying gas	180°C
P_{dry}	Pressure of the drying gas	30psi
P_{neb}	Pressure of the nebulising gas	15psi
R	Protein solution flow rate	4 μ l/min

Table I. Typical values used during ESI and ion optics

minimal m/z selectivity, to permit simultaneous and non-discriminative transport of a broad range of bio-/chemical species. The configuration we employ actually involves two independent hexapole ion guide stages. The top hexapole, operating in the 10 mTorr vacuum range, provides collisional cooling and trapping of the ions and relies on space charge for injection through an orifice into the vacuum chamber of the main cryostat. The bottom hexapole operating in high vacuum plays a dual role. It acts as an ion “pipe”, enabling broadband, high-efficiency transmission of ions over the 2m path. It is also key in overcoming the magnetic mirror effect that would otherwise reflect the ions back along their initial path as they tried to enter the high magnetic field region^{12,13}. (As described below, we have employed well-validated magnetomotive displacement transduction for the NEMS in this first generation system; it provides optimal sensitivity in a high magnetic field.) Both hexapoles are driven by a homemade RF oscillator^{14,15} that can supply AC voltages of up to 500V_{peak}. In brief, the RF power supply is based on two vacuum tubes operating in a push-pull oscillator configuration, driving an LC load formed by the capacitive load of the hexapole rods and high-voltage inductor and capacitors to tune to the frequency of oscillation. The significant length of the lower hexapole sets an upper limit to the frequency that can effectively be applied by the voltage source, though this upper limit did not come into play for the large mass species probed in this experiment. The NEMS mass sensor is centered about 3mm below the bottom end of the hexapole guide.

NEMS Device Fabrication

The structural material for the ultrahigh frequency (UHF) NEMS devices in this work is a 100nm thick single crystal 3-C silicon carbide (SiC) epilayer deposited on a silicon substrate through molecular beam epitaxy¹⁶. Thin-film metal conductors are defined by optical lithography to form wirebond pads and a lead-frame that converges into the central, active region of each device where the NEMS are located. Each of these small chips is manually diced for subsequent individual processing. Electron-beam lithography is used to laterally define what ultimately become nanometer-scale NEMS features on the SiC epilayer. Thermal evaporation is used to deposit 40nm of Al followed by 5nm Ti on these patterns, and standard lift-off is then employed to define the metallization layer. This metallization layer connects to the larger aforementioned lead-frame, and also serves as a mask for the subsequent etching process. The metal-masked SiC epilayer is etched in an Ar/NF₃ plasma created by an electron cyclotron resonance (ECR) plasma-etching system. This dry etch step removes the SiC in unprotected regions and undercuts the silicon beneath the masked SiC, to result in a fully

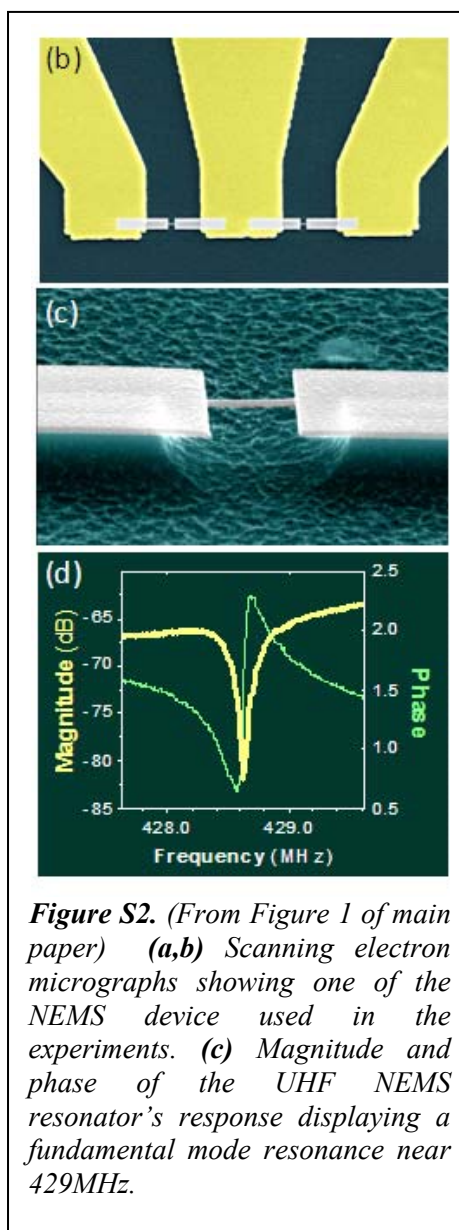


Figure S2. (From Figure 1 of main paper) (a,b) Scanning electron micrographs showing one of the NEMS device used in the experiments. (c) Magnitude and phase of the UHF NEMS resonator's response displaying a fundamental mode resonance near 429MHz.

suspended NEMS beam¹⁷. The completed devices, such as depicted in Figure S2, are geometrically characterized by a scanning electron microscope (SEM).

The NEMS mass sensor used in these measurements is a 100nm thick, doubly-clamped silicon carbide beam $\sim 1.7\mu\text{m}$ long, $\sim 120\text{nm}$ wide. In addition to its function as an etch mask, the topmost, thin-film metallization layer subsequently enables sensitive and well-validated magnetomotive actuation and transduction¹⁸.

NEMS Mass Sensor Characterization

Data presented in this work are obtained with devices such as described previously, which flexurally vibrate in-plane, with a typical fundamental mode resonance at $\sim 450\text{MHz}$ and quality factor of ~ 2000 . A typical response curve is shown in Figure S2 (panel c).

Prior to embedding candidate devices in the UHF phase locked loop (PLL) circuitry each is fully characterized electromechanically, in vacuum. This involves immersion in, typically, a 7T magnetic field and execution of the RF drive frequency sweeps with a network analyzer to locate the various NEMS electromechanical resonances. Each resonant mode observed is verified to be electromechanical in nature by confirming its expected dependence upon magnetic field ($\propto B^2$) and drive power, which is taken well into the non-linear mechanical regime¹⁹.

The temperature dependence of the fundamental-mode resonance is characterized by sweeping the sample stage temperature slowly from 25K to 65K, while recording the NEMS frequency. The resulting curve has an inverted-“U” shaped curve. We find that in the temperature range between 35K and 40K the NEMS fundamental resonance frequency is least sensitive to the temperature changes. This reduced temperature coefficient is an additional motivation for our operation at 40K; in this regime we have verified that thermal fluctuations and thermalization of landing proteins have negligible effect on the NEMS resonant frequency.

RF characterization

To determine the temporal stability of the phase locked loop we run the system in closed loop for extended time periods and determine the resulting Allan deviation. Figure S3 shows a typical plot of Allan deviation versus measurement integration time. In the flat region between 3-30 seconds the Allan deviation is limited by the $1/f$ noise. For longer measurement times drift becomes the major source of instability; for shorter times white noise dominates.

NEMS Mass Responsivity

The dynamics of a flexural mode NEMS resonator can be modeled as a simple damped harmonic oscillator²⁰. Referring to the coordinate system introduced in Figure 2 in the main text and

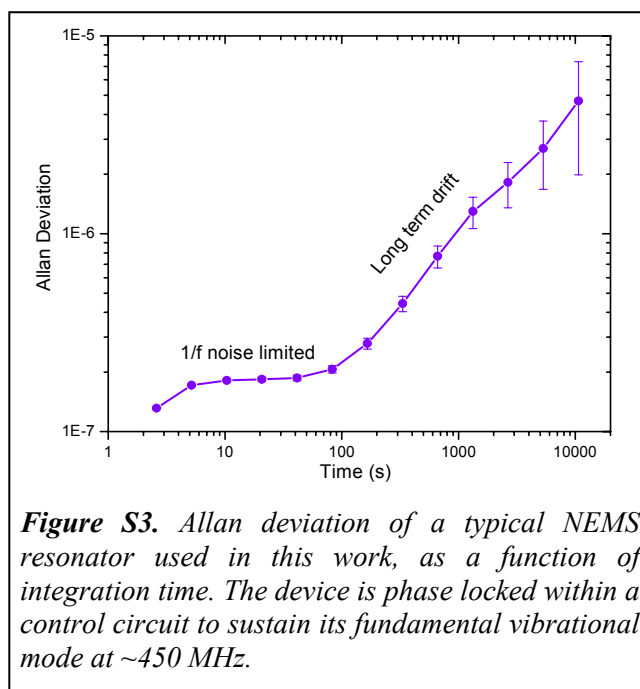


Figure S3. Allan deviation of a typical NEMS resonator used in this work, as a function of integration time. The device is phase locked within a control circuit to sustain its fundamental vibrational mode at $\sim 450\text{ MHz}$.

$$P.E. = \frac{1}{2}ky_{center}^2, \quad K.E. = \frac{1}{2}M_{eff}\dot{y}_{center}^2,$$

$$f_{nems} = \frac{1}{2\pi}\sqrt{\frac{k}{M_{eff}}}$$

Here y_{center} denotes the center-of-beam displacement, k denotes the modal stiffness coefficient, and M_{eff} denotes the modal mass of the fundamental mode, f_{nems} is the resonance frequency of the flexural mode.

At this point, it is illuminating to show how modal mass can be calculated. The mechanical resonator oscillating with a certain amplitude, $y(t)$, and angular frequency, ω , possesses kinetic energy. This kinetic energy can be calculated by considering infinitesimal slices of material along the length of the beam and summing up their infinitesimal kinetic energies:

$$K.E. = \frac{1}{2}\int dm \dot{y}^2 = \frac{1}{2}\int_{x=0}^{x=L} \rho A dx [\dot{y}(x)]^2$$

Here dm is the mass of the each infinitesimal slice considered, y is the displacement of the beam at that point, ρ is the mass density, A is the cross section of the beam and L is its length.

The displacement at a point x along the beam can be expressed as: $y(x) = y_{center} \times \varphi(x)$, where $\varphi(x)$ is the mode shape. Using this relationship:

$$K.E. = \frac{1}{2}\int_{x=0}^{x=L} \rho A dx [y_{center} \times \varphi(x)]^2 = \frac{1}{2}\left[\rho AL \frac{1}{L}\int_{x=0}^{x=L} [\varphi(x)]^2 dx\right] y_{center}^2$$

The expression inside the large square brackets is the modal mass, M_{eff} . For point mass loading of a doubly clamped beam the effective mass is given by²¹,

$$M_{eff} = M_{total} \times \frac{1}{L}\int_{x=0}^{x=L} [\varphi(x)]^2 dx = 0.397 M_{total}$$

When a point mass, δm , is added to the resonator, at a point x' along the beam, the total kinetic energy carried by the resonator will change, as the added mass is forced to oscillate with the beam. The new kinetic energy is given as:

$$K.E. = \frac{1}{2}M_{eff}\dot{y}_{center}^2 + \frac{1}{2}\delta m [\dot{y}(x')]^2$$

Using $y(x') = y_{center} \times \varphi(x')$, the above equation translates into:

$$K.E. = \frac{1}{2}M_{eff}\dot{y}_{center}^2 + \frac{1}{2}\delta m \dot{y}_{center}^2 [\varphi(x')]^2 = \frac{1}{2}[M_{eff} + \delta m[\varphi(x')]^2] \times \dot{y}_{center}^2$$

Thus, the resonator's effective mass is changed to $M_{eff} + \delta m[\varphi(x')]^2$. This in turn changes the resonance frequency:

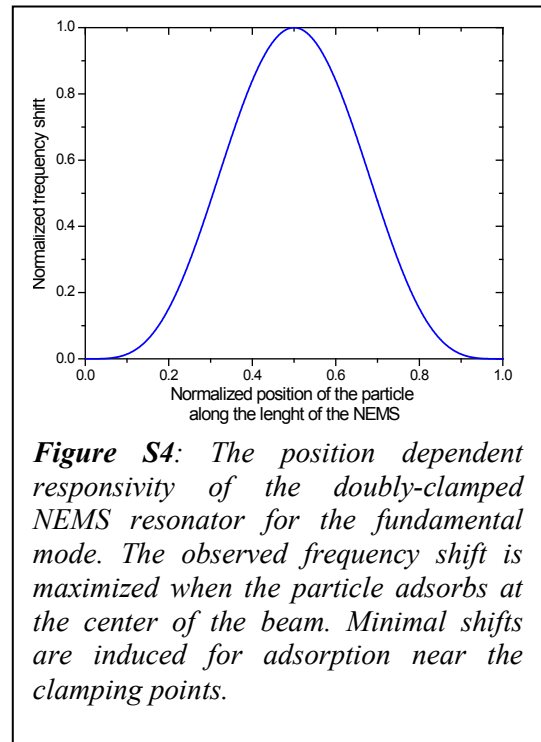


Figure S4: The position dependent responsivity of the doubly-clamped NEMS resonator for the fundamental mode. The observed frequency shift is maximized when the particle adsorbs at the center of the beam. Minimal shifts are induced for adsorption near the clamping points.

$$f'_{nems} = \frac{1}{2\pi} \sqrt{\frac{k}{M_{eff} + \delta m [\varphi(x')]^2}}$$

For $M_{eff} \gg \delta m$, as in our experiment, one can make a Taylor expansion of the square bracket to arrive at the frequency shift caused by the added mass:

$$\Delta f = f_{nems} - f'_{nems} = \left\{ -\frac{1}{2} \frac{f_{nems}}{M_{eff}} [\varphi(x')]^2 \right\} \delta m$$

The expression in the curly bracket is the position-dependent responsivity of NEMS:

$$\mathfrak{R} \equiv \frac{\delta f}{\delta M} = -\frac{f_{nems}}{2 M_{eff}} [\varphi(x')]^2$$

The shape of the position dependent responsivity is shown in figure S4.

As an example, we now calculate the responsivity for a point particle landing at the center of the beam. For this case $\varphi(x') = 1$.

The NEMS beam used in the experiment is 1.7 μm long, 120 nm wide and containing three layers: 100 nm SiC ($\rho=3.2 \text{ g/cm}^3$), 40 nm Al ($\rho = 2.7 \text{ g/cm}^3$), and 5 nm Ti ($\rho=4.5 \text{ g/cm}^3$)

Thus:

$$M_{total} = 92 \cdot 10^{-15} \text{g} = 92 \text{ fg}$$

and

$$\mathfrak{R} = -\frac{f_{nems}}{2 M_{eff}} = 6.2 \frac{\text{Hz}}{\text{zg}}$$

The experimentally observed mass responsivity of 12 Hz/zg is reasonably close to this calculated value.

Based on the experimentally-measured mass responsivity, we deduce that mass of the beam to be $M_{total}=46\text{fg}$. Using this experimentally-observed total mass, and an *upper* bound to our typical Allan deviation, $\sigma_A(\sim 5\text{sec}) \sim 3.5 \times 10^{-7}$, we deduce the following upper bounds to our mass sensitivity δM and the frequency instability for these experiments²:

$$\delta M = 2\sqrt{2} M_{eff} \sigma_A(\tau) \sim 10 \text{kDa}$$

$$\delta f = \delta M / (2 M_{eff}) f_{nems} \sim 250 \text{Hz}$$

Control runs

To verify that the change in resonant frequency of the NEMS is due to mass loading from protein molecules or nanoparticles landing on the NEMS, we perform the following three distinct control runs while tracking the resonant frequency of the NEMS:

1. Turn off the syringe pump delivering the protein solution to the ESI needle. Keep all ESI voltages and ion optics control voltages on. Proteins do not reach the ESI needle, hence protein ions should not be produced (beyond rare events arising from the dislodging of sparse protein residue accumulated within the needle, etc. – *i.e.* from previous NEMS-MS runs.
2. Turn off the ESI needle voltage. All the other parameters are kept the same as for ESI injection during regular NEMS-MS operations. In this case although the protein solution is ejected from the ESI needle due to the flow pressure generated by the syringe pump and the nebulising gas flow, the resulting droplets are not charged and any proteins, if produced, will not be transported to the NEMS by the ion guide.
3. Run the ESI with the clean solvent devoid of analytes. Assuming that there are no leftover proteins in the ESI system (as described in #1 above) we should see minimal change in the resonant frequency of the NEMS.

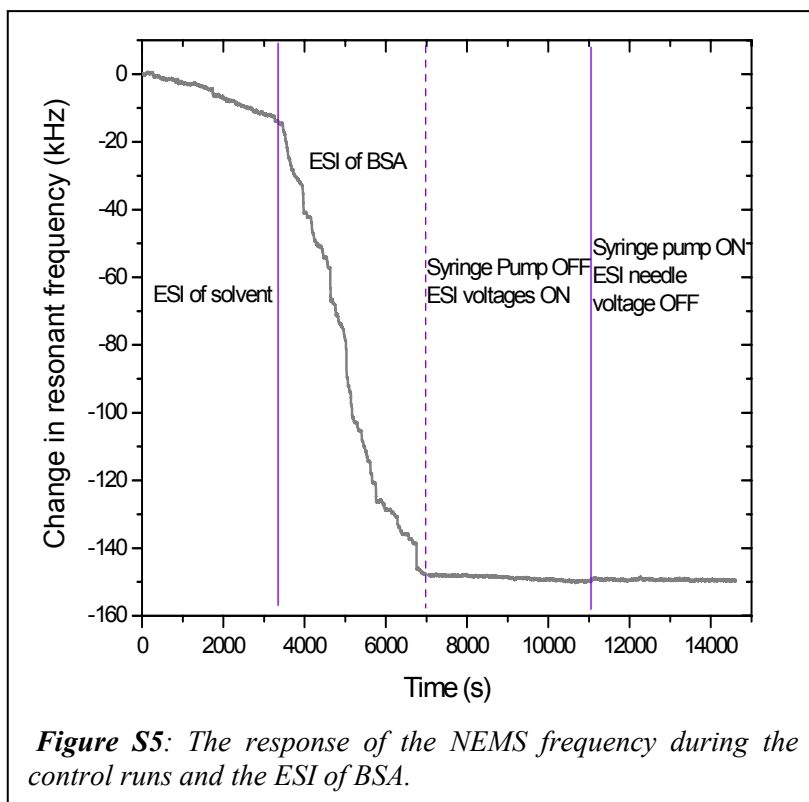


Figure S5: The response of the NEMS frequency during the control runs and the ESI of BSA.

Figure S5 shows one such time record of the resonant frequency of the NEMS during the ESI of Bovine Serum Albumin (66kDa) and three different control runs. The resonant frequency of the NEMS changes radically during the ESI of BSA protein. The frequency change is composed of scores of frequency jumps similar to the ones shown in Figure 2. During the control runs, however, the total change in resonant frequency is noticeably smaller. This indicates that the mass loading indeed arises from the protein ions produced during ESI. We believe the mass loading of the NEMS during solvent-only ESI is largely due to proteins remaining in the ESI system from previous runs. The resonant frequency changes during the other two control runs are minimal and compare well with the frequency fluctuations observed due to background gas molecules.

Cross-checks: ensuring that frequency-shift “events” indeed arise from nanoparticle/protein adsorption

One distinguishing feature of the ESI process is that it typically produces species with mass-to-charge ratios of order $m/z \sim 1000$. This can be easily verified in our experiments. Based on the relative cross-sectional area of the faraday cup and the NEMS, and using the charge-to-mass transformation, we can deduce the expected frequency shift due to mass loading of the NEMS convert from the current observed at Faraday cup. Figure S6 shows the frequency change of the NEMS due to mass loading and the expected frequency change assuming several different average m/z values.

Adsorption-event curve-fitting analysis

In order to construct frequency-shift histograms from the experimental time records of resonance frequency while under phase-lock, one needs an objective method to identify adsorption events and measure the magnitude of their corresponding frequency shifts, Δf . We have developed a Matlab script to serve this purpose. The experimental time records consist of scores of discrete frequency jumps. We characterize each of these jumps by the maximum slope at the jump center and zero slopes at the edges. Our Matlab routine scans the experimental data for local regions of high slope, subject to the conditions that our frequency-shift threshold is set to be $\Delta f \geq 2 \times \delta f$, records the experimental data as a frequency step. (As described in the main text, δf is the frequency resolution). By these procedures the extracted frequency jumps are “filtered” to reject both impulsive noise spikes and long term drifts. Practically, this is achieved by putting lower and upper limits on the acceptable time-scale of “real” frequency jumps. Later, each frequency jump data in this filtered set is fitted to the modeled time-response of the PLL circuitry as described in the main text. The parameters in this PLL model are chosen initially from circuit analysis and validated by separate measurements. These circuit parameters are iteratively varied slightly to obtain the best fit between the experimental characterization measurements and calculated PLL temporal response function (see main text, Figure 2b). The heights of the frequency jumps obtained during the fitting process are

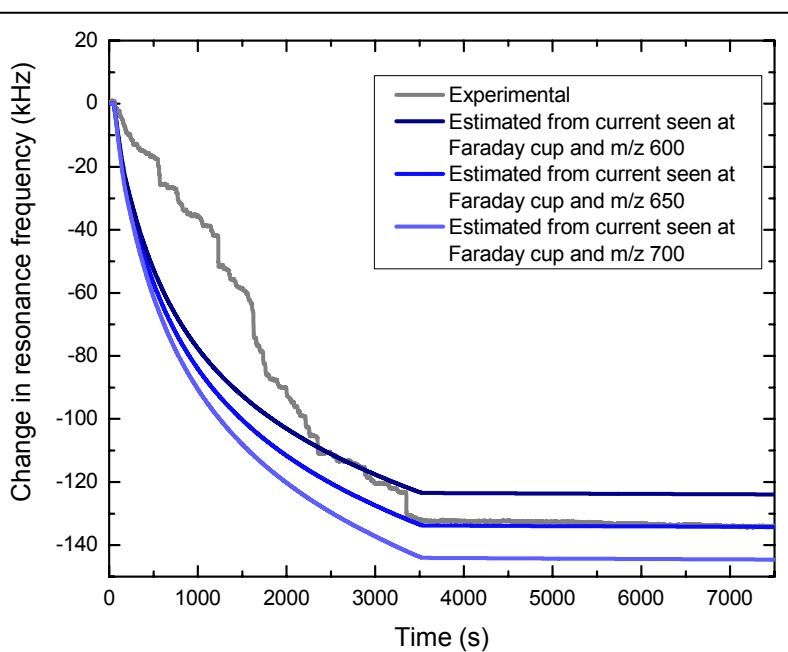


Figure S6. The frequency change observed during the experiment (gray solid line) and the frequency change expected based on the ionic current measured at the faraday cup. The expected curve is calculated by assuming an average m/z of 600, 650 and 700 and converting it into mass deposited on the NEMS.

recorded and used to construct the experimental event-probability histograms.

Histograms during “analysis” and “control” runs

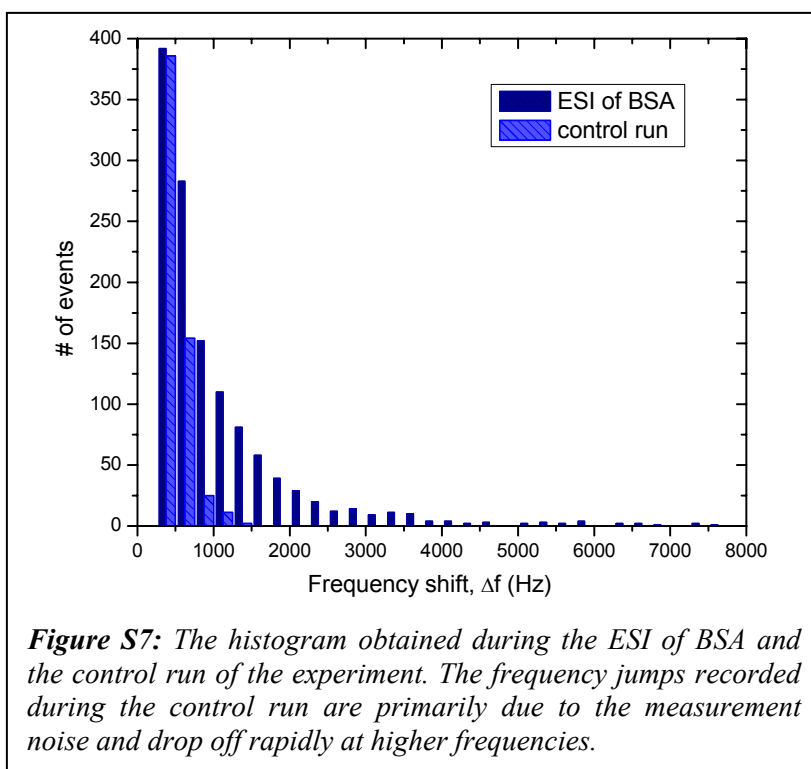
Each NEMS-MS protein or nanoparticle analysis run is followed by a control run of roughly the same time scale. During these control runs the syringe pump is shut off and all other controls of the system are maintained as during the corresponding analysis run. Due to the frequency-fluctuation noise of the phase-locked NEMS, a finite number of abrupt frequency jumps will be counted even during the control run. We generate separate histograms of the jumps obtained during the analysis runs and the control runs. Typical histograms for the analysis and the control runs from NEMS-MS for BSA are shown in figure S7. The histograms from control runs are then used to perform background subtraction from the histogram obtained from the corresponding analysis runs.

Calculation of the ion transmission transfer function for the hexapole ion guides.

To determine the efficiency of ion transmission from the ESI source to the NEMS as a function of mass/charge ratio we numerically simulated the transmission properties of our system (using the SIMION software). The results of the simulations for three different hexapole frequencies are shown in figure S8.

With the hexapole operating at a frequency of 1.1 MHz, the ion optics of our system favor the transmission of ions with m/z in the range from 100 to 1000, while for a lower hexapole frequency (450kHz) they favor transmission of ions with larger m/z (see figure S8). During the positive ESI process used for proteins, protonation occurs at the basic residue sites of the proteins. The resulting m/z spectra tend to be bell shaped curves, and the maximum charging state observed is consistent with the number of basic residues expected for small proteins^{22,23}. However, for large proteins (similar to the ones used in our experiments), as the number of charges accumulated increases, Columbic repulsion prevents basic residue sites from acquiring additional charge²⁴. Furthermore, for larger proteins the basic amino acids buried within the protein structure tend to be inaccessible to the more acidic liquid and/or gas phase molecules. Thus larger proteins generally have larger m/z values.

We can easily verify the above



hypothesis by obtaining the frequency shift histograms for β -amylase with hexapole operating at frequencies 1.1 MHz and repeating the experiments with 450 kHz. Based on SIMION simulations, we expect that the higher hexapole frequency would preferentially transmit ions with low m/z and hence of lower mass. This would translate into a larger low frequency peak at a higher hexapole frequency. The experimental results are shown in figure S9. Note that the probability of observing a low mass ($\Delta f < 1.5$ kHz) event is dramatically reduced when the hexapole frequency is changed from 1.1 MHz to 450 kHz. In addition, the probability of observing larger frequency shifts (larger mass) is also significantly improved at 450 kHz.

NEMS-MS of β -amylase

We show results from one additional NEMS-MS experiment on a protein sample. Figure S10 shows the results obtained from ESI of β -amylase with a hexapole drive frequency of 450 kHz. The event probability histogram displays a broad peak at 3600Hz, which we associate with the β -amylase monomer. Sweet potato β -amylase is known to be a tetramer of identical subunits²⁵ and under a variety of experimental conditions the protein molecules can fragment into

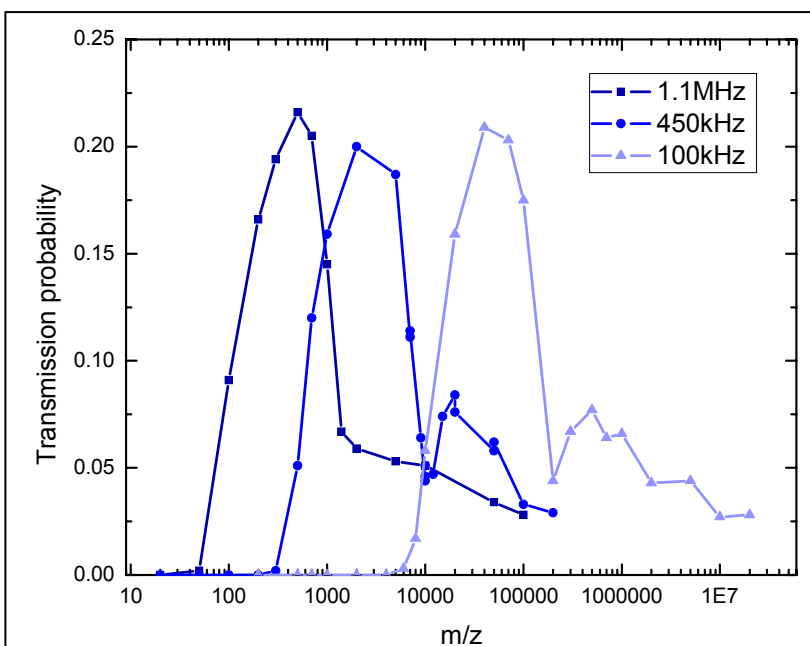


Figure S8. Transmission probability of the ions through the ion optics. The plot clearly shows the preference for low m/z transmission with higher hexapole frequency.

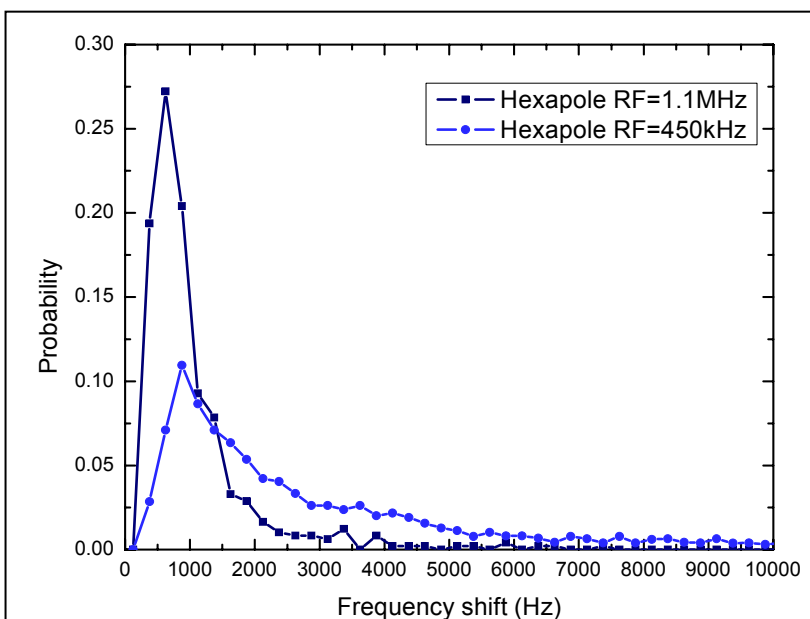


Figure S9. Plot of probability of frequency shifts during electrospray ionization of β -Amylase. Notice the dramatic change in the relative heights at low frequency. This indicates that the hexapole RF frequency of 1.1 MHz favors the transmission of low mass ions. Also visible are the shoulder at about 3.5kHz corresponding to β -Amylase monomers landing close to the center of the NEMS.

individual subunits²⁶. We believe the broadening of the monomer peak, as well as the absence of a clear bicuspid shape in the histogram, arise from the presence of such protein subunits in these experiments. As shown by the curve “decomposition” in Figure S10, the experimental histogram can be readily explained by assuming a weighted superposition of subunits.

Data analysis procedure used to construct first-generation NEMS-MS spectra.

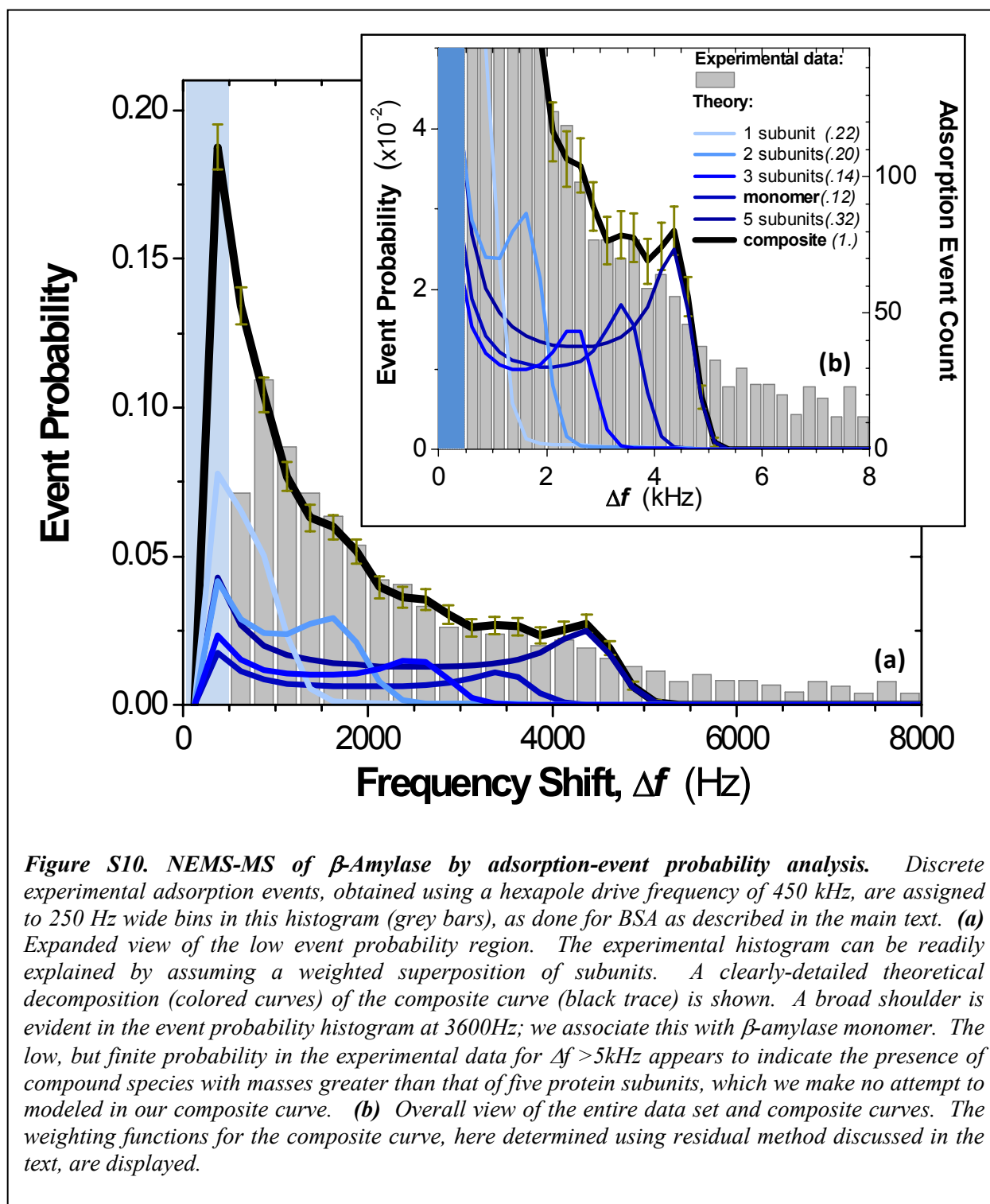
To provide an unbiased extraction of our first NEMS-MS mass spectra from the experimentally obtained event-probability histograms, we fit the experimental data to realistic models. These models are based on predicted NEMS-MS event-probabilities assuming the injection of multicomponent mixtures – in these experiments, sample solutions containing either a Au nanoparticle dispersion, a family of BSA oligomers, or a family of re-aggregated β -amylase subunits. These fits are provided in an unbiased manner through automated procedures that allow the relative intensities of the sample’s components to be deduced. We treat the intensities of the solution components as variable parameters, and use the minima of the sum-of-squared-errors (SSE) to determine the relative intensities of the (variable-radius) nanoparticles or molecular species that adsorb upon the NEMS. We now describe the specific examples presented in this initial NEMS-MS work.

Calculation of the SSE

Gold: We generate a theoretical histogram from 1 million adsorption events. This histogram assumes a normalized mass of 1 for the nanoparticle and includes the effect of our finite, 250Hz frequency resolution. We vary the mean radius of the gold nanoparticles in steps of 0.01nm from 1.9nm to 2.9 nm and the standard deviation in steps of 0.003nm from 0.2nm to 0.75nm. Theoretical histograms are generated by “rescaling” the master histogram for each value of the mean radius and the standard deviation. Each theoretical histogram is then compared against the experimental histogram to calculate the SSE for each specific radius/deviation value. The contour map of Figure 3c (main text) represents the SSE’s determined in this manner.

BSA: A theoretical histogram of 100,000 events is generated similar to the one for the gold. In this case we assume that the protein solution is composed of five oligomers: monomers, dimers, trimers, tetramers, and pentamers. We adjust the fractional intensities of the monomer, dimer, trimer and pentamer event probability in steps of 0.01 and calculate the resulting SSE between the resulting theoretical histogram and the data. Fine adjustments of the tetramer value, the weakest peak in the experimental curve, are carried out to maintain the total weight of unity. We weight the SSE to suppress the effect of the freq shifts < 500Hz which are deemed experimentally unreliable (as these are heavily biased by NEMS frequency-fluctuation noise; see main text for discussion.) For each set of oligomer probabilities, we “rescale” the calculated histogram and compare it with the experimental histogram to calculate the SSE. On the next page Figure S11 shows the fit residues from the ten two-dimensional cuts through the five-dimensional SSE optimization space.

β -Amylase: A theoretical histogram of 100,000 events is generated, similar to the one for the gold. In this case we assume that the protein is composed of monomer and the other four of its first five re-aggregated subunits. The subunits themselves can aggregate to form particles of higher mass. Here we change the monomer and subunit event probabilities in steps of 0.02. As for BSA, the SSE in this case are weighted to reduce the effect of the freq shifts < 500Hz. As for the previous examples each set of probabilities for the oligomers, we “rescale” the histogram and compare it with the experimental histogram to calculate the SSE. A graphical representation of this optimization process, not shown here, is similar in appearance to Figure S11.



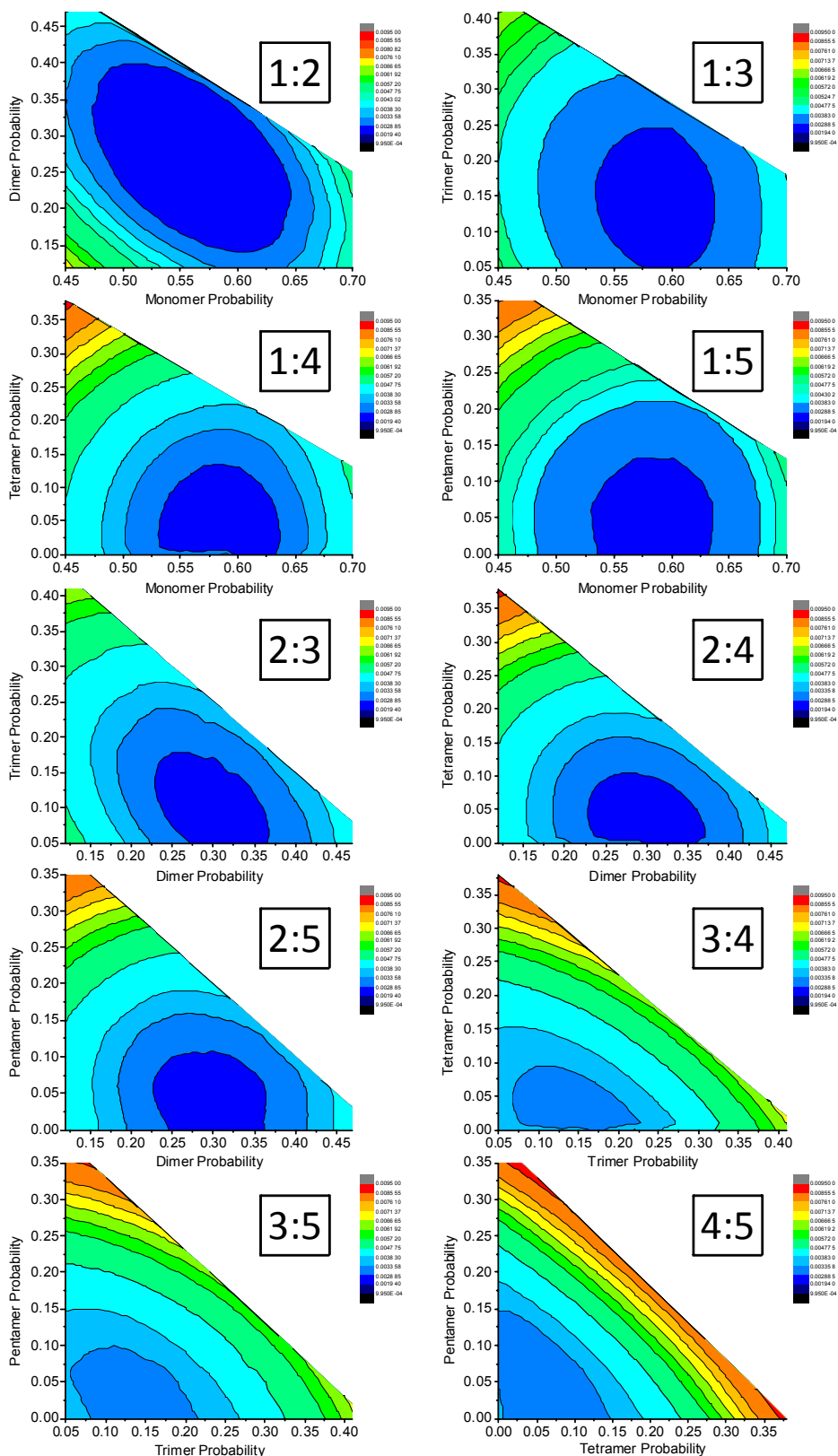
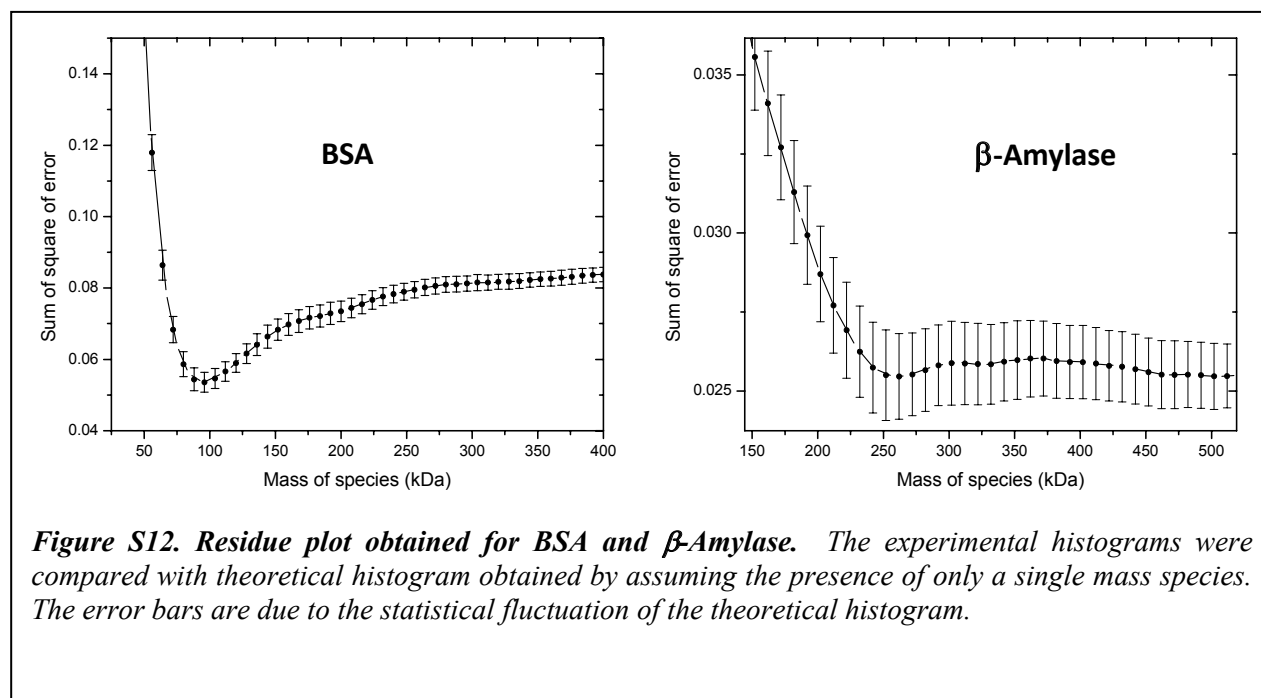


Figure S11. Optimization of weighting coefficients for mass spectrum of BSA and its oligomers. Each subplot shows the variation of the SSE as we vary the event probability of the various oligomers. Note that the optimization was obtained by varying the probability of all the oligomers. The plots are two dimensional snapshots of the entire optimization process.

Analysis of BSA and β -Amylase assuming presence of single species:

As an alternative procedure to the analyses of protein described above, where the presence of multiple species has been assumed, we also have analyzed our experimentally-obtained histograms by assuming that only a single mass species is present in solution. We then compare the resulting theoretical histogram with the experimental histogram to obtain the SSE, and carry out this procedure for a range of analyte mass. As seen in figure S12, the SSE shows a minimum for a mass of approximately 95kDa for BSA. This is fairly close to the average mass value of 118kDa obtained by summing the weighted average of the intensities obtained in Figure 4.

A similar analysis of β -Amylase gives a SSE minimum at \sim 250kDa. The minimum for this protein is rather shallow, hence mass determination by this approach is less conclusive.



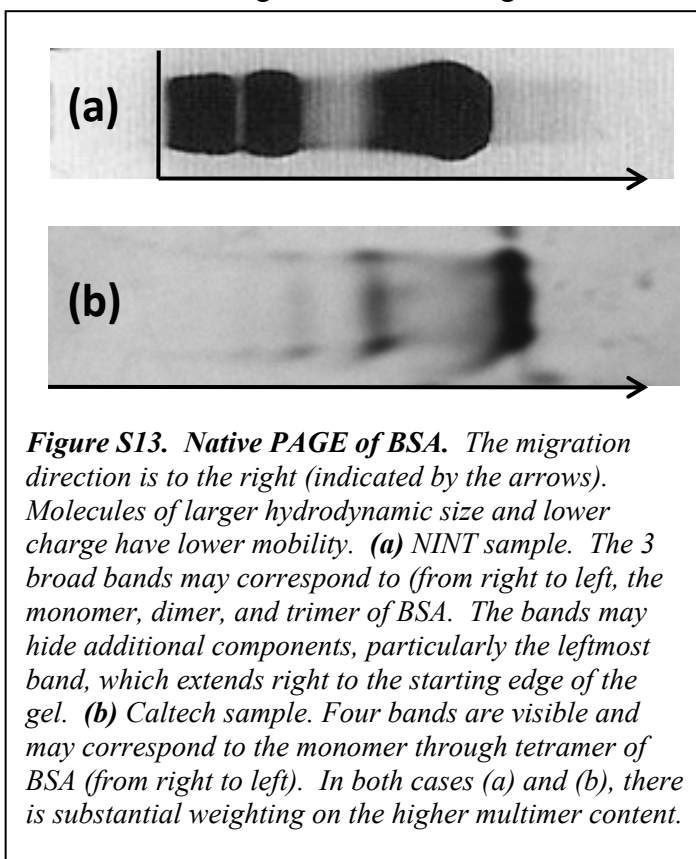
Native gel electrophoresis of BSA

There is significant precedent for the high degree of multimerization in the NEMS-MS spectra we observe. This has been previously elucidated in studies of non-covalent interactions using ESI-MS²⁷⁻³⁰. Indeed, in Ref. 29 the same BSA monomer-to-dimer ratio of 2:1, as deduced from our NEMS-MS method, was previously observed.

To further confirm high multimer content in our samples, we have analyzed our BSA sample solution by performing native polyacrylamide gel electrophoresis (native PAGE). Figure S13 shows native PAGE gels of different BSA samples performed at NINT (Edmonton) and at Caltech. The Caltech BSA sample is from the same lyophilized powder used in the NEMS-MS experiment and prepared at the same molarity. Both samples show several distinct bands that

likely correspond to different multimers of BSA with the rightmost band being the monomer. Note that the density in the multimer bands is a significant fraction of the total density. This appears to imply that there is a rather high degree of multimerization.

However, two points of caution should be noted: (i) Native PAGE cannot provide a direct, straightforward connection between the observed electrophoretic mobility and mass; many additional factors contribute to analyte mobility. (ii) The ESI process parameters employed in our experiments themselves can alter the degree of species aggregation; hence this can be different than that of the condensed state in fluid. Hence, we view these results of the native PAGE as corroborating, but not proving, that a high degree of multimerization exists in our sample solution.



References:

- 1 Ekinci, K.L., Huang, X.M.H., & Roukes, M.L., Ultrasensitive nanoelectromechanical mass detection. *Appl. Phys. Lett.* **84**, 4469-4471 (2004).
- 2 Feng, X.L., Ph.D. Dissertation, California Institute of Technology, 2006.
- 3 Feng, X.L., White, C.J., Hajimiri, A., & Roukes, M.L., A self-sustaining ultrahigh-frequency nanoelectromechanical oscillator. *Nature Nanotech.* **3**, 342-346 (2008).
- 4 Yang, Y.T., Callegari, C., Feng, X.L., Ekinci, K.L., & Roukes, M.L., Zeptogram-scale nanomechanical mass sensing. *Nano Lett.* **6**, 583-586 (2006).
- 5 Yamashita, M. & Fenn, J.B., Electrospray ion source. Another variation on the free-jet theme. *J. Phys. Chem.* **88**, 4451-4459 (1984).
- 6 Fenn, J.B., Mann, M., Meng, C.K., Wong, S.F., & Whitehouse, C.M., Electrospray ionization for mass spectrometry of large biomolecules. *Science* **246**, 64-71 (1989).
- 7 Dass, C., *Fundamentals of Contemporary Mass Spectrometry*. (Wiley-Interscience, 2007).
- 8 Douglas, D.J. & French, J.B., Collisional focusing effects in radio frequency quadrupoles. *J. Am. Soc. Mass Spectrom.* **3**, 398-408 (1992).
- 9 Chernushevich, I.V. & Thomson, B.A., Collisional Cooling of Large Ions in Electrospray Mass Spectrometry. *Anal. Chem.* **76**, 1754-1760 (2004).
- 10 Kantrowitz, A. & Grey, J., A High Intensity Source for the Molecular Beam. Part I. Theoretical. *Rev. Sci. Instrum.* **22**, 328-332 (1951).

- 11 Whitehouse, C.M., Dreyer, R.N., Yamashita, M., & Fenn, J.B., Electrospray interface for
liquid chromatographs and mass spectrometers. *Anal. Chem.* **57**, 675-679 (1985).
- 12 Lebrilla, C.B., Amster, I.J., & McIver, R.T., External ion source FTMS instrument for
analysis of high mass ions. *Int. J. Mass Spectrom. Ion Processes* **87**, R7-R13 (1989).
- 13 McIver Jr., R.T., United States Patent No. **4535235** (1985).
- 14 Ronald, M.J. & Scott, L.A., Simplified radio-frequency generator for driving ion
guides, traps, and other capacitive loads. *Rev. Sci. Instrum.* **71**, 4335-4337 (2000).
- 15 Ronald, M.J., Dieter, G., & Scott, L.A., Simple radio-frequency power source for ion
guides and ion traps. *Rev. Sci. Instrum.* **68**, 3357-3362 (1997).
- 16 Zorman, C.A. *et al.*, Epitaxial growth of 3C--SiC films on 4 in. diam (100) silicon
wafers by atmospheric pressure chemical vapor deposition. *J. Appl. Phys.* **78**, 5136-
5138 (1995).
- 17 Yang, Y.T. *et al.*, Monocrystalline silicon carbide nanoelectromechanical systems.
Appl. Phys. Lett. **78**, 162-164 (2001).
- 18 Cleland, A.N. & Roukes, M.L., Fabrication of high frequency nanometer scale
mechanical resonators from bulk Si crystals. *Appl. Phys. Lett.* **69**, 2653-2655 (1996).
- 19 Postma, H.W.C., Kozinsky, I., Husain, A., & Roukes, M.L., Dynamic range of nanotube-
and nanowire-based electromechanical systems. *Appl. Phys. Lett.* **86**, 223105-
223103 (2005).
- 20 Cleland, A.N., *Foundations of Nanomechanics: From Solid-State Theory to Device
Applications*. (Springer Verlag, 2002).
- 21 Karabacak, D.M., Ph.D. Dissertation, Boston University, 2008.
- 22 Covey, T.R., Bonner, R.F., Shushan, B.I., Henion, J., & Boyd, R.K., The determination of
protein, oligonucleotide and peptide molecular weights by ion-spray mass
spectrometry. *Rapid Commun. Mass Spectrom.* **2**, 249-256 (1988).
- 23 Smith, R.D., Loo, J.A., Edmonds, C.G., Barinaga, C.J., & Udseth, H.R., New developments
in biochemical mass spectrometry: Electrospray ionization. *Analytical Chemistry
(Washington) ; Vol/Issue: 62:9; DOE Project*, Pages: 882-899 (1990).
- 24 Loo, J.A. & Loo, R.R.O., *Electrospray Ionization Mass Spectrometry of Peptides and
Proteins*. (John Wiley & Sons 1997).
- 25 Cheom Gil Cheong *et al.*, Crystallization, molecular replacement solution, and
refinement of tetrameric beta-amylase from sweet potato. *Proteins: Struct., Funct.,
Genet.* **21**, 105-117 (1995).
- 26 Justin L. P. Benesch, Brandon T. Ruotolo, Douglas A. Simmons, & Robinson, C.V.,
Protein Complexes in the Gas Phase: Technology for Structural Genomics and
Proteomics. *ChemInform* **38** (2007).
- 27 Light-Wahl, K.J., Schwartz, B.L., & Smith, R.D., Observation of the Noncovalent
Quaternary Associations of Proteins by Electrospray Ionization Mass Spectrometry.
JACS **116**, 5271-5278 (1994).
- 28 Joseph A. Loo, Observation of large subunit protein complexes by electrospray
ionization mass spectrometry. *J. Mass Spectrom.* **30**, 180-183 (1995).
- 29 Yang Wang, M.S., Arnd Ingendoh, Jochen Franzen,, Analysis of non-covalent protein
complexes up to 290 kDa using electrospray ionization and ion trap mass
spectrometry. *Rapid Commun. Mass Spectrom.* **14**, 12-17 (2000).
- 30 Loo, J.A., Electrospray ionization mass spectrometry: a technology for studying
noncovalent macromolecular complexes. *Int. J. Mass Spectrom.* **200**, 175-186 (2000).